Contents lists available at ScienceDirect

Applied Catalysis B: Environmental

Boosting photocatalytic activity of Pd decorated TiO$_2$ nanocrystal with exposed (001) facets for selective alcohol oxidations

Jinguo Wang, Pinhua Rao, Wei An, Jingli Xu, Yong Men*

College of Chemistry and Chemical Engineering, Shanghai University of Engineering Science, Shanghai 201620, PR China

A B S T R A C T

Pd decorated TiO$_2$ nanocrystal with exposed (001) facets was synthesized *via* solvothermal hydrolysis combining photoreduction deposition route, which exhibited a great enhancement in activity and stability of photocatalytic selective alcohol oxidations under UV light irradiation in aqueous medium. The superior activity of Pd decorated TiO$_2$ nanocrystal with exposed (001) facets was attributed to the synergistic promoting effects of the following factors: firstly, the exposed (001) facets with higher surface energy facilitated the activation of reactant molecules and the photocatalytic oxidation; secondly, the increased oxygen vacancies and enhanced O$_2$ adsorption on (001) facets could trap photoelectrons and thus, inhibit their recombination with holes; thirdly, the decoration with Pd nanoparticles effectively reduce the photocharge recombination rate by capturing photoelectrons. Meanwhile, this photocatalyst displayed excellent durability owing to the strong Pd-TiO$_2$ interaction against deactivation caused by either Pd leaching or Pd aggregation.

© 2016 Elsevier B.V. All rights reserved.

1. Introduction

With increasing concerns on environmental and energy issues caused by the utilization of non-regeneratable fossil fuels, photocatalysis has been widely studied owing to its potential applications in environmental cleaning and energy generation [1–9]. Until recently, studies have been conducted on the application of photocatalytic organic synthesis. In particular, selective oxidations of alcohols to their corresponding aldehydes or ketones by photocatalysis represented one of the most important reactions both from aspects of fundamental and practical research, and have received much attention to meet the urgent demand for green organic synthesis [7–9]. Compared with traditional processes carried out in environmentally harmful organic solvents and heavy metal reagents (*e.g.* Cr and Mn salts or V$_2$O$_5$) or moisture-sensitive oxidants [10–13], photocatalytic oxidation conducted under mild conditions without using toxic solvents and reagents is regarded as one promising route for green and sustainable organic synthesis.

The photocatalyst plays the key role in determining the photocatalytic efficiency. To date, TiO$_2$ is the most widely used semiconductor in heterogeneous photocatalysis because of its earth abundance, low toxicity, and strong stability [1–3]. Both theoretical prediction and experimental results reveal that TiO$_2$ with high surface area favored the rapid diffusion and adsorption of reactant molecules [1–3]. Meanwhile, it has also been demonstrated that TiO$_2$ with high crystallinity exhibits a high photoactivity due to the rapid transfer of photoelectrons and thus, inhibiting their recombination with holes [1,14]. Obviously, TiO$_2$ nanocrystal may function as an ideal photocatalyst owing to its high surface area and high crystallinity. Since photocatalytic reactions occur on the catalyst surface, the exposed crystal facets of catalysts significantly affected the photcatalytic efficiency. Recently, TiO$_2$ nanocrystals with uniform and well-defined morphologies were synthesized, and the effect of different crystal facets on photocatalytic activity was investigated. TiO$_2$ with exposed (001) facets exhibited higher activity which is associated with its high surface energy and abundant oxygen vacancies [15–20]. Accordingly, TiO$_2$ nanocrystal with controllably exposed (001) facets is expected to be the more active photocatalyst.

Very recently, modification of TiO$_2$ nanocrystal with noble metals has been demonstraed to be efficient alternative approach for improving photocatalytic efficiency owing to the noble metals facilitating the interfacial electron transfer [21–24]. Among various noble metals, metallic Pd is most frequently employed in selective aerobic oxidation of alcohols due to its high activity and selectivity [25–28]. Xu et al. have shown that the enhanced photocatalytic performance of Pd@CdS nanocomposite in selective oxidation of alcohols was ascribed to the coupling interaction of enhanced

---

light-harvesting and the longer lifetime of photogenerated charge carriers [27]. Despite the great activity of selective photooxidation of alcohols achieved over Pd@CdS nanocomposites, the potential structual instability of CdS upon exposure of light irridiation and use of organic solvent imposed limitaions of its wide application as practical catalyst. To the best of our knowledge, the deposition of Pd nanoparticles on well-defined TiO_2 nanocrystals and investigation of their shape-dependent photocatalytic performance in selective photooxidation of alcohols are not yet reported in the open publications.

Herein, Pd decorated TiO_2 nanocrystal with exposed (001) facets was synthesized *via* solvothermal hydrolysis and subsequent photoreduction deposition route. The results demonstrated that this photocatalyst exhibited high activity and strong durability in photocatalytic selective oxidation of aromatic alcohols to their corresponding aldehydes under UV light irradiation in relation to the synergetic promoting effects, indicating good potential in practical applications.

2. Experimental

2.1. Sample preparation

TiO_2 nanocrystal with exposed (001) facets was prepared by solvothermal hydrolysis. Typically, 50 mL tetrabutyl titanate was mixed with 8.0 mL HF under stirring at room temperature, and then transferred into a 100 mL autoclave and kept at 180 °C for 24 h. The products were collected by centrifugation, washed with distilled water and dried at 80 °C for 10 h, and the obtained sample was denoted as T001. TiO_2 nanocrystal with exposed (101) facets was also synthesized *via* solvothermal hydrolysis as follows: 15 mL tetrabutyl titanate was mixed with 60 mL acetic acid under stirring at room temperature, and then transferred into a 100 mL autoclave and kept at 200 °C for 24 h. The products were collected by centrifugation, washed with distilled water and dried at 80 °C for 10 h, and the obtained sample was denoted as T101.

Loading Pd nanoparticles: 1.0 g T001 or T101 was added into a mixed solution containing 80 mL H_2O, 10 mL methanol and 5.0 mL H_2PdCl_4 (20 mmol/L) aqueous solution under stirring, and then high-purity N_2 was bubbled into the suspension for 30 mins to remove O_2. After that, the suspension was irradiated by a 100 W UV-LEDs with characteristic wavelength (λ) of 365 nm for 3.0 h under N_2 atmosphere. The obtained samples were collected by centrifugation, washed with distilled water and dried at 80 °C for 10 h, and finally denoted as PT001 and PT101, respectively.

2.2. Characterization

The loading of Pd nanoparticles was determined by inductive coupled plasma emission spectrometer (ICP, Varian, VISTAMPX-ICP). The crystal structure and morphology were characterized by X-ray diffraction (XRD, Rigacu D/Max-2000, monochromatic CuKα radiation) and high-resonance transmission electron microscopy (HRTEM, JEOL JEM-2100). N_2 adsorption-desorption isotherms were determined on Micromeritics ASAP 2460 at 77 K, from which, surface area (S_{BET}), pore volume (V_P) and pore diameter (D_P) were calculated by applying Brunauer-Emmett-Teller (BET) and Barrett-Joyner-Halenda (BJH) models on the desorption branches. The surface electronic states were analyzed by X-ray photoelectron spectroscopy (XPS, PerkinElmer PHI 5000). All the binding energy values were calibrated by using $C_{1s} = 284.6$ eV as the reference. Raman spectra, photoluminescence spectroscopy (PLS), and UV–vis diffuse reflectance spectra (UV–vis DRS) were collected on a Dilor Super LabRam Π, Varian Cary-Eclipse 500, and MC-2530, respectively. The oxygen temperature-programmed desorption (O_2-TPD) curves were obtained on a Micromeritics Autochem II 2920 instrument equipped with a thermal conductivity detector (TCD). The 0.10 g of catalysts were placed in U-shaped fixed-bed quartz microreactor, and pretreated at 260 °C for 30 min with ultrahigh He flow of 50 mL/min, and then exposed to pure O_2 for 90 min at 30 °C. After that, the catalysts were flushed in ultra-high He flow to remove the physically absorbed O_2, and then heated up to 600 °C with a heating rate of 10 °C/min. The released O_2 was
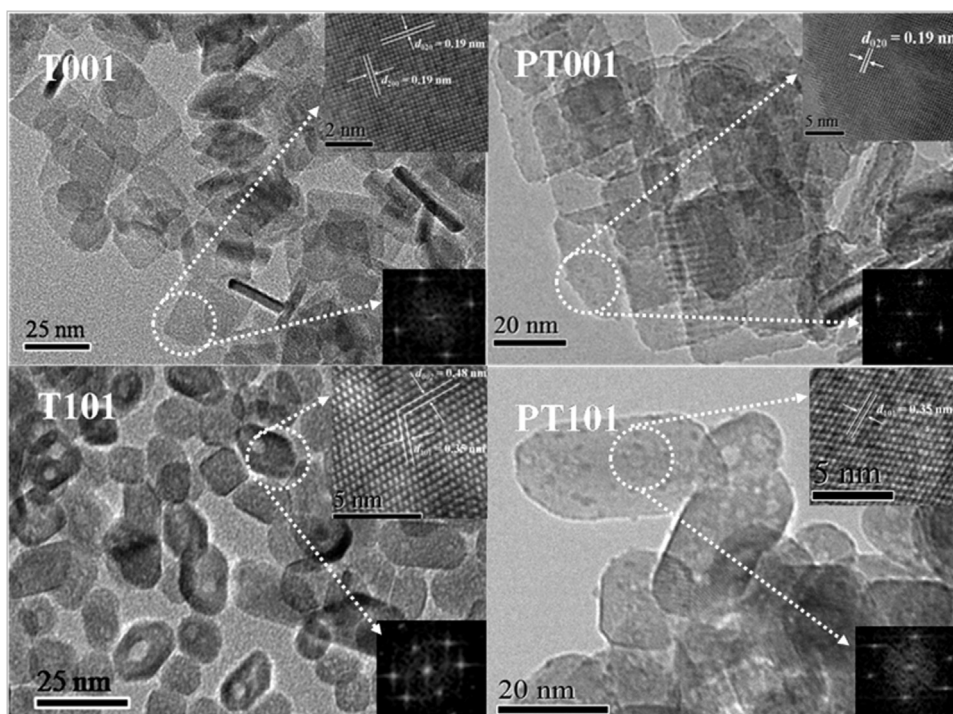

Fig. 1. TEM images of different samples; the insets are the corresponding HRTEM and fast-Fourier transform (FFT) images, respectively.

determined by the TCD. The photocurrent measurements were performed in a homemade three-electrode quartz cell containing 0.20 mol/L Na_2SO_4 aqueous solution with a PAR VMP3Multi Potentiotat apparatus and a BAS Epsilon workstation, and the system was equipped with a 100 W UV-LEDs with characteristic wavelength (λ) of 365 nm. The Pt plate and the Ag/AgCl electrode were used as the counter and reference electrodes, respectively, while the work electrode was prepared by depositing 10 mg photocatalyst onto fluoride-tin oxide (FTO) conductor glass. The products of the photocatlytic selective oxidation of aromatic alcohols to their corresponding aldehydes were detected by GC–MS (Agilent 6890N/5973I).

2.3. Activity test

The photocatalytic selective alcohol oxidations were carried out in a self-designed 100 mL reactor containing 0.10 g catalysts, 10 mL H_2O, and 0.10 mmol benzyl alcohol or its derivatives. All reactions were conducted at 25 °C in a static O_2 atmosphere (1.0 atm) under irradiation by a 100 W UV-LEDs with characteristic wavelength (λ) of 365 nm mounted at 5.0 cm away from the reactor. After reaction for 2.0 h, the reaction products were extracted with diethylether and analyzed using a gas chromatograph (Shimadzu, GC-2014). Blank experiments demonstrated that negligible oxidations occurred in the absence of either light irradiation or catalysts. The capturing experiment of active species was also conducted using the same method by charging 10 mmol of different scavengers. The reproducibility of all the activity tests was checked by repeating each result at least three times and was found to be within acceptable limits (±3%).

3. Results and discussion

3.1. Structural characteristics

The TEM images in Fig. 1 revealed that the T001 and PT001 were both present in nanosheets with an average length around 25 nm and thickness about 5.0 nm whereas the T101 and PT101 displayed octahedrons morphology with an average size of 20 nm. The corresponding HRTEM and FFT images reveal that all the samples were present in well-defined anatase TiO_2 single crystal with predominantly exposed (001) facets on the T001 and PT001, and (101) facets on the T101 and PT101. Meanwhile, the loading of Pd metal onto TiO_2 support generated Pd nanoparticles with an average size about 3.0 nm.

Fig. 2 demonstrated that all the samples displayed the typical type IV N_2 adsorption-desorption isotherms (IUPAC classification) with H3 hysteresis loops at relative pressure range of 0.80–1.0, indicating the typical mesoporous structure [14,18] In aligned with non-porous structure as evidenced by TEM images in Fig. 1, the observed mesopores were mainly attributed to the aggregated voids by self-assembly of TiO_2 nanocrystal units. The corresponding pore size distribution curves indicated that all the samples owned an average pore diameter around 14 nm. Based on the N_2 adsorption-desorption isotherms, the S_{BET}, V_p, and D_p (see Table 1) have been calculated by using BET and BJH models, respectively. It could be clearly seen that all the samples possessed similar surface area, while the surface area and pore size almost kept unchanged after introducing the low mass loading of Pd.

The XRD patterns in Fig. 3 displayed that all the samples were present in anatase phase with high crystallization degree, corresponding to the 2θ of 25.8°, 37.7°, and 47.8° indicative of (101), (004), and (200) diffractions (JCPDS No.12-1272) [1–3]. No diffraction peaks of individual Pd particles could be observed because of its low loading or small size. Meanwhile, the (004) peaks of T001
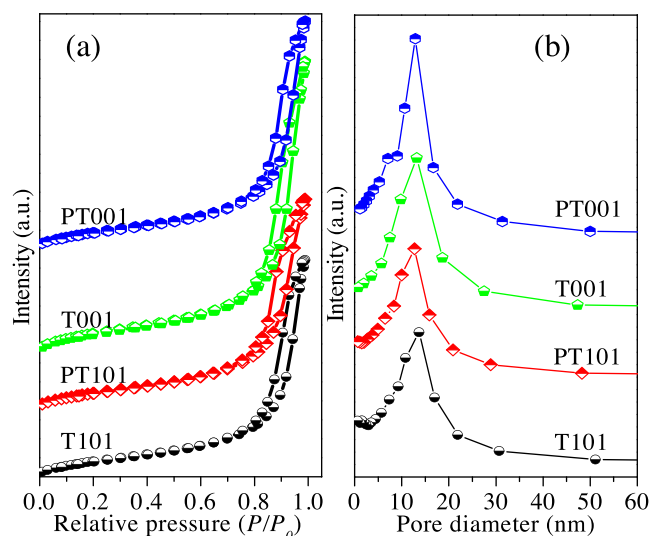

Fig. 2. N_2 adsorption-desorption isotherms (a) and pore size distribution curves (b) of different samples.
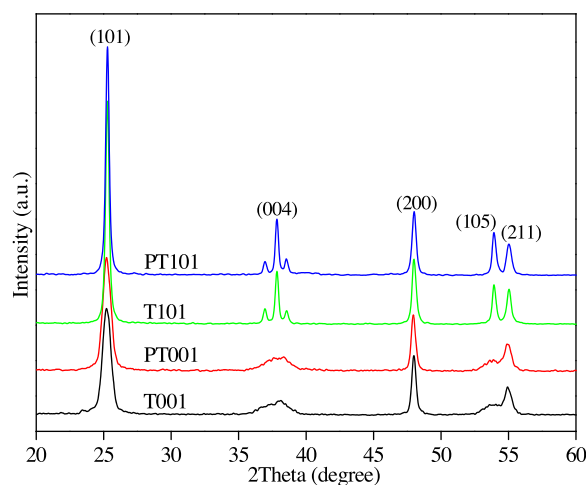

Fig. 3. XRD patterns of different samples.

and PT001 were broader than that of T101 and PT101, suggesting that the crystal growth along the [001] axis vertical to (001) facets was inhibited in T001 and PT001. Taking into account the fact that the (001) facets were formed by the deformation growth of anatase TiO_2 crystal from octahedron to decahedron (see Scheme S1), the percentage of (001) facets would increase if the up and down crystal growth was inhibited, corresponding to the small "h" and big "m" values. According to the intensities (*i.e.*, the half-height width) of (004) and (101) peaks, the crystallite sizes along the [001] and [101] axis vertical to (001) and (101) facets, *i.e.*, the "h" and "m" values in the crystal model were calculated by Scherer's equation, based on which the percentage of exposed (001) facets could be calculated [14,18]. As shown in Table 1, the T101 and PT101 exposed only about 8.0% of (001) facets while as a greater extent, *i.e.*, 80% of (001) facets were exposed on the T001 and PT001.

The Raman spectra in Fig. 4 showed that all the samples exhibited the peaks at 144 cm^{-1} (E_g), 394 cm^{-1} (B_{1g}), 514 cm^{-1} (A_{1g}), and 636 cm^{-1} (E_g), which are the characteristics of the anatase TiO_2 phase. However, the magnified Raman spectra from 120 to 180 cm^{-1} (see the inset) clearly evidenced a positive shift of the principal peak by about 3.5 cm^{-1} over the T001 and PT001 as compared with that of T101 and PT101, indicative of an increase in the number of surface oxygen vacancies on (001) facet [29,30]. This can

Table 1
Physical structural parameters of different samples.

Sample	Pd loading (wt%)	S_{BET} (m^2 g^{-1})	V_p (cm^3 g^{-1})	D_p (nm)	Crystal size (nm)	Exposed (001) (%)
T101	/	110	0.46	12	19	8.0
PT101	0.99	106	0.44	13	19	7.9
T001	/	119	0.51	13	12	80
PT001	0.97	114	0.48	14	12	80
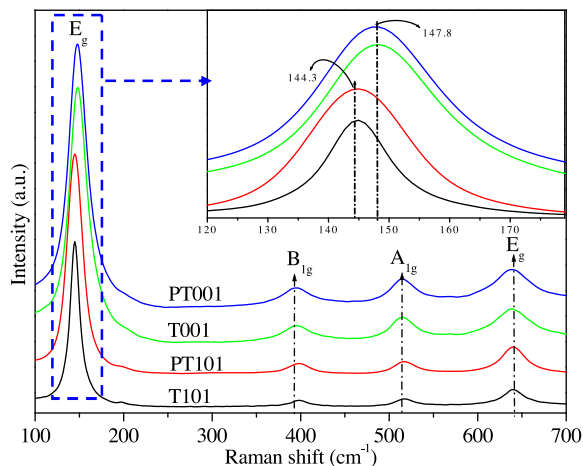
Fig. 4. Raman spectra of different samples; the inset shows the magnified Raman spectra from 260 to 380 nm.
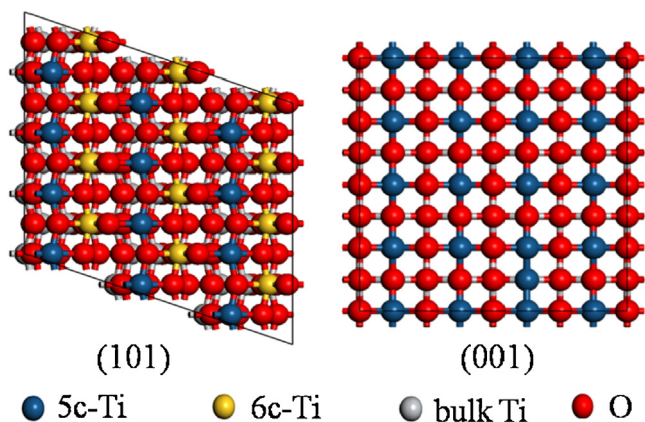
Fig. 5. The atomic structure model of anatase TiO$_2$ (101) and (001) surfaces.

be attributed to the different coordination numbers of Ti atom in the (001) and (101) facets (see Fig. 5). Ti atom in (001) facets is in 5-fold coordination, but in (101) facets, Ti atom is coordinated with either 5 or 6 oxygen atoms, with an equal probability [31]. It can be expected the (001) facets have more abundant surface oxygen vacancies in comparison with the (101) facets due to the more low-coordinated Ti atom with oxygen on the surface. In connection with XRD results, the XRD patterns in Fig. 3 revealed that the T001 and PT001 contained a significantly higher extent of (001) facets than those on T101 and PT101, which also accounted for the enhanced number of oxygen vacancies on T001 and PT001.

The XPS spectra of Pd$_{3d}$ in Fig. 6 exhibited that the doublet peaks at the binding energy of 335.2 and 340.5 eV corresponding to the Pd$_{3d5/2}$ and Pd$_{3d3/2}$, respectively, which can be assigned to the metallic form of Pd [27,32]. However, the binding energy of Ti^{4+} in T001 and PT001 shifted negatively by around 0.50 eV with regards to that of T101 and PT101, while the binding energy of O^{2-} in T001 and PT001 shifted positively by around 0.40 eV, which also indicated the enhanced number of surface oxygen vacancies [14,19].

The O$_2$-TPD profiles in Fig. 7 clearly displays a larger amount of desorbed oxygen from T001 than T101, evidencing more abundant oxygen vacancies on the exposed (001) facets, in good accordance with the Raman and XPS characterization results.

Fig. 8 illustrated that the photocurrent generated under light irradiation on all the samples and decayed rapidly to zero when the light irradiation was turned off, indicating that all the samples functioned as semiconductors to produce photoelectrons under light irradiation. Notably, the photocurrent intensity varied in the order of PT001 > PT101 > T001 > T101. Taking into account the fact that all the samples were present in anatase phase with nearly the same energy band gap (3.2 eV), the photocurrent intensity was mainly dependent on the light-harvesting ability and the separation efficiency of photocharges. The light-harvesting ability of was examined by UV–vis-DRS as shown in Fig. 9, which exhibited all the samples displayed almost the same absorption profile with a steep absorption edge around 385 nm corresponding to the characteristic energy band gap of 3.2 eV about anatase TiO$_2$. However, the magnified UV–vis DRS spectra from 260 to 380 nm clearly showed the difference in the UV range with the varied order of absorption capability in PT001 > PT101 > T001 > T101. Taking into account the fact that all the samples have the similar surface area, this could imply that it's not the key influencing factor. Thus, the stronger light-harvesting of T001 and PT001 than the corresponding T101 and PT101, respectively, was attributed to the different energy levels because of the (001) facets with a lower energy band gap (3.18 eV) than the (101) facets (3.22 eV) [17,31]. Meanwhile, the PT001 and PT101 exhibited stronger light-harvesting than the corresponding T001 and T101, which was mainly attributed to the strong Pd-TiO$_2$ interaction. The PLS spectra in Fig. 10 revealed that the intensity of PL emission around 560 nm went down in the order of T101 > T001 > PT101 > PT001, indicating the decrease in the recombination rate between photoelectrons and holes [19,21,29]. The T001 and PT001 exhibited a lower recombination rate between photoelectrons and holes than that on corresponding T101 and PT101 counterparts, due to the smaller crystallite size and abundant surface oxygen vacancies. On one hand, the smaller crystallite size of T001 and PT001 facilitated the rapid transfer of photoelectrons, which diminished the transfer distance of photoelectrons and thus, prohibited their recombination with holes. On the other hand, the T001 and PT001 with more exposed (001) facets contained more surface oxygen vacancies, and therefore captured photoelectrons and thus, inhibited their recombination with holes. It is worthwhile to note that, the PT001 and PT101 exhibited lower recombination rate between photoelectrons and holes as compared to the corresponding T001 and T101, ascribing to that Pd nanoparticles may function as electron sinks to trap the photoelectrons and thus decrease their recombination with holes.

3.2. Photocatalytic performance

The selective oxidation of alcohols to their corresponding aldehydes is widely recognized as one of the most important functional group transformations used in fine chemicals [25–28,33–36]. As a typical example, the photocatalytic selective oxidation of benzyl alcohol to benzaldehyde was initially investigated over PT001. The HPLC–MS analysis revealed the negligible formation of side-
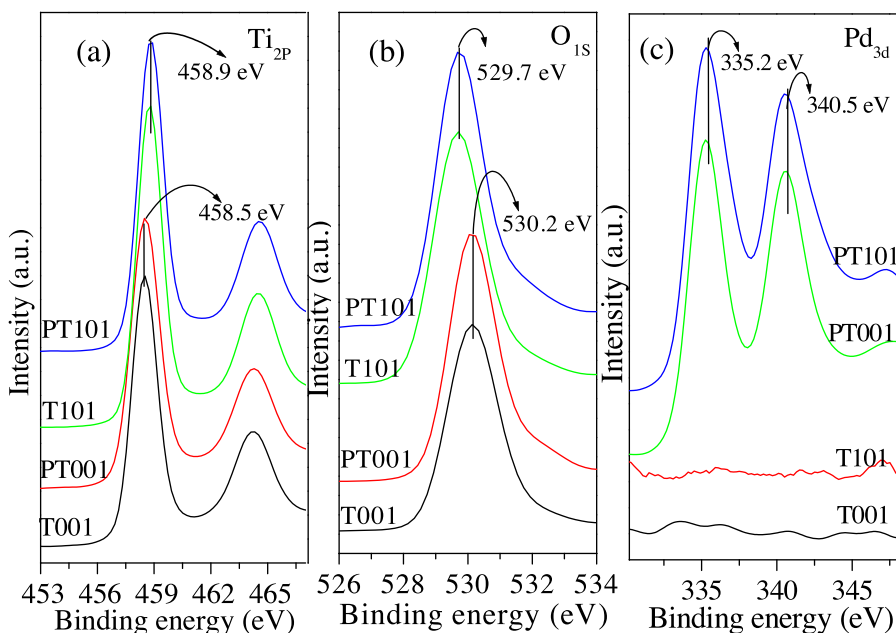
Fig. 6. XPS spectra of different samples: Ti_{2p} of (a), O_{1s} of (b) and Pd_{3d} of (c).
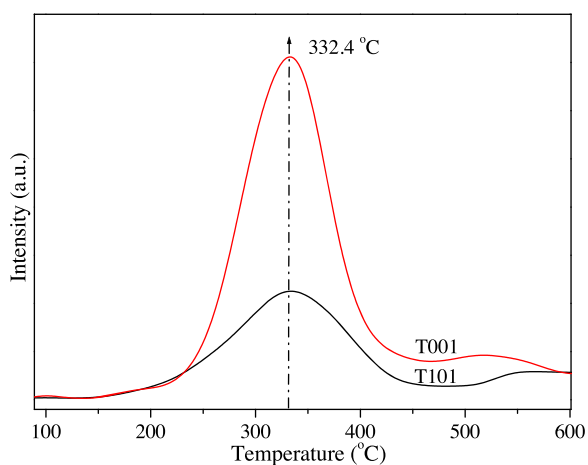

Fig. 7. O_2 temperature-programmed desorption curves of different samples.
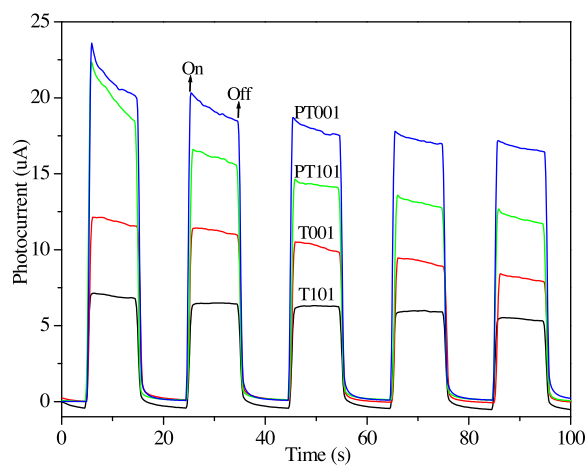

Fig. 8. Photocurrent responses of different samples.

products other than its corresponding aldehyde, suggesting the absolute selectivity toward the target product under the present conditions. Meanwhile, different captures were added before the initiation of reaction to examine the key active intermediate species in the present photocatalytic oxidation. As shown in Fig. 11, as an effective $^\bullet$OH radicals scavenger [37], the terephthalic acid addition didn't bring any substantial down in activity, indicating that $^\bullet$OH radicals were not involved in photocatalytic oxidation. However, a dramatical decrease in activity was observed by adding either methanol to capture photogenerated holes (h^+), or $AgNO_3$ to capture photoelectrons (e^-), or benzoquinone to capture $^\bullet O_2{}^-$ radicals, or bubbling N_2 to remove the dissolved O_2 [38–40]. These results afforded the evidences that, except for $^\bullet$OH radicals, the photogenerated holes (h^+), photoelectrons (e^-) and $^\bullet O_2{}^-$ radicals were actively engaged as the main active species in the present oxidation reaction. A tentative reaction mechanism was schematically outlined in Fig. 12. Firstly, TiO_2 semiconductor produced photoelectrons (e^-) and holes (h^+) under UV light irradiation. Then the holes activated the absorbed benzyl alcohol to generate benzyl alcohol cation radicals, and the photoelectrons transferred to Pd nanoparticles from the conductive band of TiO_2 and subsequently facilitated
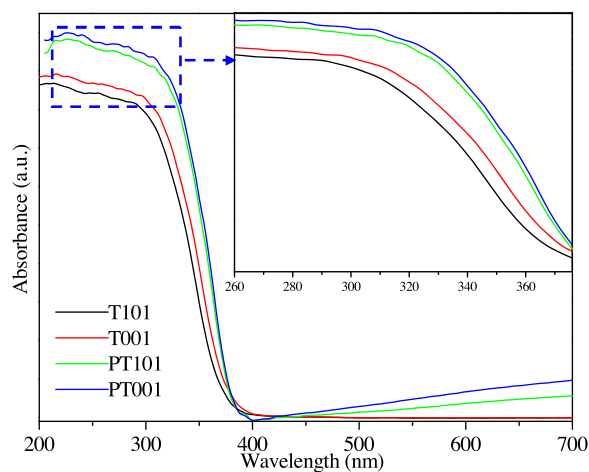

Fig. 9. UV–vis DRS spectra of different samples; the inset exhibits the magnified UV–vis DRS spectra from 260 to 380 nm.
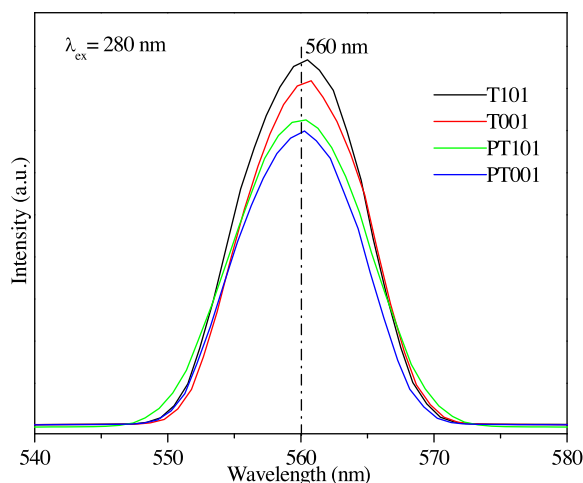
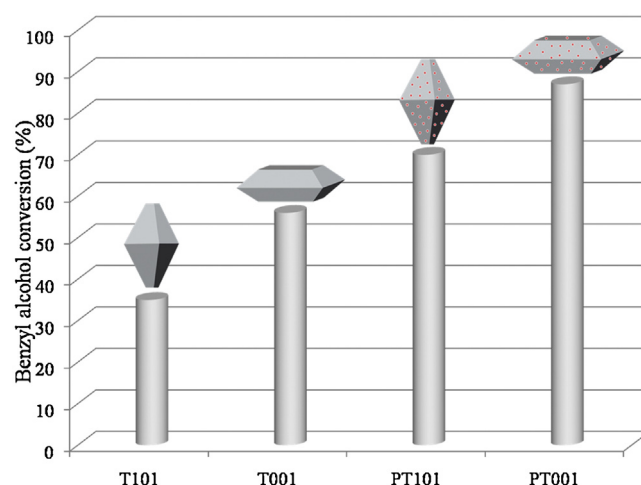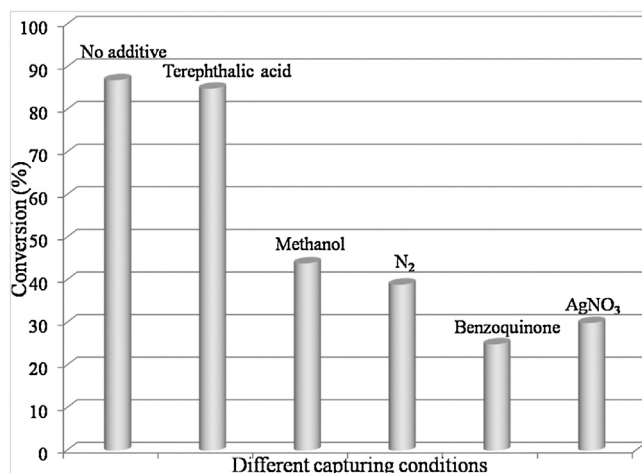Fig. 10. PLS spectra of different samples.

Fig. 11. Photocatalytic performances of PT001 for the selective oxidation of benzyl alcohol in the presence of different capturers.
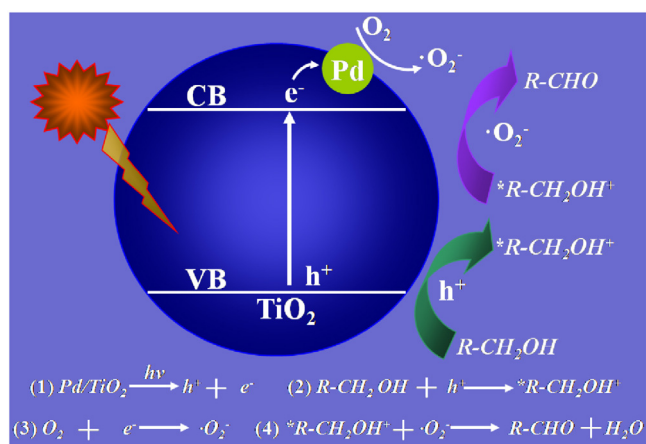

Fig. 12. A plausible mechanism for photocatalytic selective oxidation of aromatic alcohols to their corresponding aldehydes.
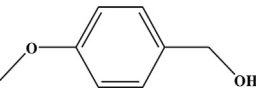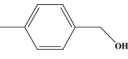
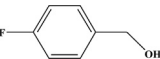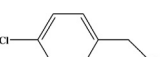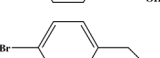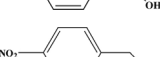the activation of the dissolved O_2 by formation of the $\cdot O_2{}^-$ radicals. Finally, the $\cdot O_2{}^-$ radicals reacted with the benzyl alcohol cation radicals to produce benzaldehyde.

Fig. 13 showed that the photocatalytic activity of selective oxidation of benzyl alcohol to benzyldehyde ranked in the order

Fig. 13. Photocatalytic activity of different samples for the selective oxidation of benzyl alcohol.

of PT001 > PT101 > T001 > T101, and the same sequence was also obtained in selective oxidation of benzylic alcohols to their corresponding aldehydes (see Table 2). The catalysts in all cases gave rise to the similar product selectivity. Based on these results, two conclusions could be drawn: (1) the TiO_2 nanocrystal with exposed (001) facets exhibited higher activity than TiO_2 nanocrystal with exposed (101) facets, demonstrating a strong crystal facet-dependent reactivity; and (2) Pd nanoparticles decorated TiO_2 nanocrystal showed higher activity than pure TiO_2 nanocrystal. Since all the samples had similar surface area (see Table 1), the enhanced activity of T001 and PT001 than the corresponding T101 and PT101 must be associated with other physical and chemcial factors, *i.e.*, the crystal size, the extent of exposed (001) facets, the light-harvesting, the number of surface oxygen vacancies. The T001 and PT001 with smaller crystallite size naturally diminished the transfer distance of photoelectrons and thus reduced their recombination rate with holes. The higher exposed (001) facets of T001 and PT001 favored the photocatalytic oxidation due to its higher surface energy, and the lower energy band gap (3.12 eV) in the (001) facets than the (101) facets (3.20 eV) also enhanced the light-harvesting efficiencies. The abundant surface oxygen vacancies and enhanced O_2 adsorption in T001 and PT001 could capture photoelectrons and thus retard the recombination rate of photoelectron-hole. Meanwhile, the PT001 and PT101 exhibited higher activity than the corresponding T001 and T101, respectively, in relation to that the deposition of Pd nanoparticles acted as the electron sinks to facilitate the separation of photoelectrons from holes. From Table 2, it was quite clear that benzylic alcohols with electron-donating groups (*p-CH3* and *p-OCH3*) displayed slightly higher conversion than those with electron-withdrawing groups (*p-F*, *p-Cl*, *p-Br*, and *p-NO2*) but their selectivities were almost the same, agreeing well with the previous reported work [41]. The electron-donating groups endowed the $-CH_2OH$ moieties with higher electron cloud density than those with electron-withdrawing groups and as a consequence, the photogenerated holes interacted more easily with $-CH_2OH$ to generate the corresponding cation radicals. This could also confirm the mechanism rationality of photocatalytic selective oxidation reactions as proposed in Fig. 12.

Durability is much more important for a photocatalyst with potential practical application. To explore the durability of different samples, the photocatalyst was allowed to centrifuge after each run of reaction, followed by washing thoroughly with distilled water and ethanol, respectively. After that, the photocatalyst was retested by charging fresh reactants in subsequent recycle of photocatalytic

Table 2
Photocatalytic performances of different samples in selective oxidation of benzylic alcohols.

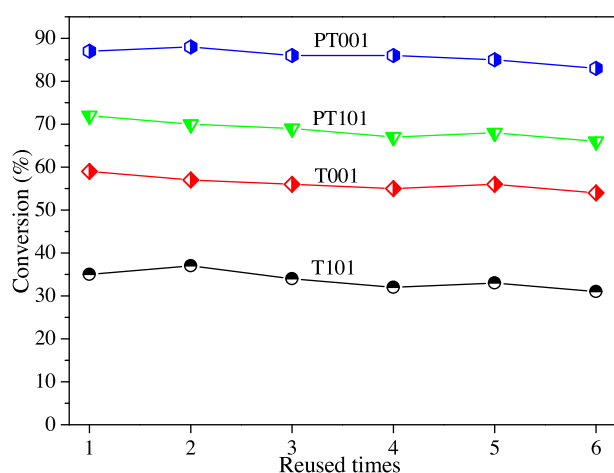| Reactant	Conversion (%)				Selectivity (%)			
	T101	T001	PT101	PT001	T101	T001	PT101	PT001
(4-methoxybenzyl alcohol)	40	63	75	93	98	99	99	98
(4-methylbenzyl alcohol)	38	60	74	92	100	99	99	98
(4-fluorobenzyl alcohol)	28	49	59	80	98	97	99	100
(4-chlorobenzyl alcohol)	30	51	62	81	99	97	100	100
(4-bromobenzyl alcohol)	32	53	64	83	99	100	100	100
(4-nitrobenzyl alcohol)	26	35	41	60	95	96	98	98

Fig. 14. Recycling test of different samples for the selective oxidation of benzyl alcohol.

reaction under the same conditions. As shown in Fig. 14, all the samples could be used repetitively at least 6 times without significant deactivation, demonstrating the high durability of all the samples in association with their high crystallization degree and the strong Pd-TiO$_2$ interaction against either Pd leaching or Pd aggregation for the PT001 and PT101 (see Fig. S1).

4. Conclusions

In summary, we have developed a facile approach for preparing Pd decorated TiO$_2$ nanocrystal with mainly exposed (001) facets, which exhibited high activity in photocatalytic selective oxidation of aromatic alcohols in aqueous medium under UV light irradiation. The superior activity of this photocatalyst was originated with the synergetic promoting effects which were in good correlation with the stronger light-harvesting, greater extent of (001) facets exposure, more surface oxygen vacancies, enhanced O$_2$ adsorption and strong Pd-TiO$_2$ interaction. Meanwhile, this photocatalyst displayed excellent durability owing to the high crystallization degree and the strong Pd-TiO$_2$ interaction against either Pd leaching or Pd aggregation, demonstrating good potential in practical applications.

Appendix A. Supplementary data

Supplementary data associated with this article can be found, in the online version, at http://dx.doi.org/10.1016/j.apcatb.2016.05.018.

References

[1] X.B. Chen, S.S. Mao, Chem. Rev. 107 (2007) 2891–2959.
[2] X.B. Chen, S.H. Shen, L.G. Guo, S.S. Mao, Chem. Rev. 110 (2010) 6503–6570.
[3] J.H. Pan, H.Q. Dou, Z.G. Xiong, C. Xu, J.Z. Ma, X.S. Zhao, J. Mater. Chem. 20 (2010) 4512–4528.
[4] M.C. Wen, M. Kohsuke, K. Yasutaka, H. Yamashita, ChemCatChem 21 (2015) 3519–3525.
[5] M.C. Wen, Y. Kuwahara, M. Kohsuke, D.Q. Zhang, H.X. Li, H. Yamashita, J. Mater. Chem. A 3 (2015) 14134–14141.
[6] M.C. Wen, K. Mori, T. Kamegawa, H. Yamashita, Chem. Commun. 50 (2014) 11645–11648.
[7] G. Palmisano, V. Augugliaro, M. Pagliaro, L. Palmisano, Chem. Commun. 43 (2007) 3425–3737.
[8] G. Palmisano, E. García-López, G. Marcì, V. Loddo, S. Yurdakal, V. Augugliaro, L. Palmisano, Chem. Commun. 46 (2010) 7074–7089.
[9] M.Q. Yang, Y.J. Xu, Phys. Chem. Chem. Phys. 15 (2013) 19102–19118.
[10] C. Aellig, C. Girard, I. Hermans, Angew. Chem. Int. Ed. 50 (2011) 12355–12360.
[11] Q. Wang, M. Zhang, C.C. Chen, W.H. Ma, J.C. Zhao, Angew. Chem. Int. Ed. 49 (2010) 7976–7979.
[12] A. Tanaka, K. Hashimoto, H. Kominami, Chem. Commun. 47 (2011) 10446–10448.
[13] D. Tsukamoto, M. Ikeda, Y. Shiraishi, T. Hara, N. Ichikuni, S. Tanaka, T. Hirai, Chem. Eur. J. 17 (2011) 9816–9824.
[14] J.G. Wang, Z.F. Bian, J. Zhu, H.X. Li, J. Mater. Chem. A 1 (2013) 1296–1302.
[15] H.G. Yang, C.H. Sun, S.Z. Qiao, J. Zou, G. Liu, S.C. Smith, H.M. Cheng, G.Q. Lu, Nature 453 (2008) 638–641.
[16] H.G. Yang, G. Liu, S.Z. Qiao, C.H. Sun, Y.G. Jin, S.C. Smith, H.M. Cheng, G.Q. Lu, J. Am. Chem. Soc. 131 (2009) 4078–4083.
[17] J. Pan, G. Liu, G.Q. Lu, H.M. Cheng, Angew. Chem. Int. Ed. 50 (2011) 2133–2137.

[18] J.G. Wang, P. Zhang, X. Li, J. Zhu, H.X. Li, Appl. Catal. B 134–135 (2013) 198–204.
[19] X.R. Li, J.G. Wang, Y. Men, Z.F. Bian, Appl. Catal. B 187 (2016) 115–121.
[20] L.Q. Ye, J. Mao, J.Y. Liu, Z. Jiang, T.Y. Peng, L. Zan, J. Mater. Chem. A 1 (2013) 10532–10537.
[21] Z.F. Bian, J. Zhu, F.L. Cao, Y.F. Lu, H.X. Li, Chem. Commun. 45 (2009) 3789–3791.
[22] N. Zhang, S.Q. Liu, X.Z. Fu, Y.J. Xu, J. Phys. Chem. C 115 (2011) 9136–9145.
[23] C.T. Dinh, H. Yen, F. Kleitz, T.O. Do, Angew. Chem. Int. Ed. 53 (2014) 6618–6623.
[24] W.J. Zhou, Y. Guan, D.Z. Wang, X.H. Zhang, X.G. Liu, H. Liu, S.W. Chen, Chem. Asian J. 9 (2014) 1648–1654.
[25] K. Mori, T. Hara, T. Mizugaki, K. Ebitani, K. Kaneda, J. Am. Chem. Soc. 126 (2004) 10657–10666.
[26] M.J. Schultz, R.S. Adler, W. Zierkiewicz, T. Privalov, M.S. Sigman, J. Am. Chem. Soc. 127 (2005) 8499–8507.
[27] N. Zhang, S.Q. Liu, X.Z. Fu, Y.J. Xu, J. Mater. Chem. 22 (2012) 5042–5052.
[28] D.I. Enache, J.K. Edwards, P. Landon, B.S. Espriu, A.F. Carley, A.A. Herzing, M. Watanabe, C.J. Kiely, D.W. Knight, G.J. Hutchings, Science 311 (2006) 362–365.
[29] J. Zhu, Y.N. Huo, H.X. Li, J. Phys. Chem. C 111 (2007) 18965–18969.
[30] J.C. Parker, R.W. Siegei, Appl. Phys. Lett. 57 (1990) 943–945.
[31] Y.B. Zhao, W.H. Ma, Y. Li, H.W. Ji, C.C. Chen, H.Y. Zhu, J.C. Zhao, Angew. Chem. Int. Ed. 51 (2012) 3188–3192.
[32] K. Fujiwara, U. Muller, S.E. Pratsinis, ACS Catal. 6 (2016) 1887–1893.
[33] G. Palmisano, S. Yurdakal, V. Augugliaro, V. Loddo, L. Palmisano, Adv. Synth. Catal. 349 (2007) 964–970.
[34] N. Zhang, S.Q. Liu, X.Z. Fu, Y.J. Xu, J. Phys. Chem. C 115 (2011) 22901–22909.
[35] Z.R. Tang, Y.H. Zhang, Y.J. Xu, ACS Appl. Mater. Interface 4 (2012) 1512–1520.
[36] M.Q. Yang, N. Zhang, Y.J. Xu, ACS Appl. Mater. Interface 5 (2013) 1156–1164.
[37] S.B. Zhu, T.G. Xu, H.B. Fu, J.C. Zhao, Y.F. Zhu, Environ. Sci. Technol. 41 (2007) 6234–6239.
[38] G.L. Huang, S.C. Zhang, T.G. Xu, Y.F. Zhu, Environ. Sci. Technol. 42 (2008) 8516–8521.
[39] J.H. Kou, Z.S. Li, Y.P. Yuan, H.T. Zhang, Y. Wang, Z.G. Zou, Environ. Sci. Technol. 43 (2009) 2919–2924.
[40] W.J. Li, D.Z. Li, J.J. Xian, W. Chen, Y. Hu, Y. Shao, X.Z. Fu, J. Phys. Chem. C 114 (2010) 21482–21492.
[41] Y.H. Zhang, N. Zhang, Z.R. Tang, Y.J. Xu, Chem. Sci. 3 (2012) 2812–2822.